

Role of electron-electron interactions in M -valley twisted transition metal dichalcogenides

Christophe De Beule,^{1,2} Liangtao Peng,³ E. J. Mele,¹ and Shaffique Adam^{3,1,4}

¹*Department of Physics and Astronomy, University of Pennsylvania, Philadelphia, Pennsylvania 19104, USA*

²*Department of Physics, University of Antwerp, Groenenborgerlaan 171, 2020 Antwerp, Belgium*

³*Department of Physics, Washington University in St. Louis, St. Louis, Missouri 63130, United States*

⁴*Department of Materials Science and Engineering,*

National University of Singapore, 9 Engineering Drive 1, Singapore 117575

(Dated: August 21, 2025)

We investigate the role of long-range Coulomb interactions in M -valley moiré systems using the self-consistent Hartree-Fock approximation. This platform was recently proposed [[Nature 643, 376 \(2025\)](#) and [arXiv:2411.18828 \(2024\)](#)] as a new class of experimentally realizable moiré materials using twisted transition metal dichalcogenides homobilayers with the 1T structure. While these seminal studies considered the noninteracting theory without an interlayer bias due to an electric displacement field, this work shows that both electron-electron interactions at finite doping and an interlayer bias strongly modify the moiré bands. For small twist angles, the density of states as a function of filling and interlayer bias shows qualitatively different behavior for twisting near aligned (0°) and antialigned (60°) stacking. More interestingly, the Van Hove singularity becomes pinned to the Fermi energy over a finite range of doping, an effect known to enhance both superconductivity and strongly correlated states. For aligned stacking this occurs only at zero electric field, while for antialigned stacking this happens both at zero and finite field. Our work demonstrates that correlated states in M -valley 1TtTMDs can be strongly tuned *in situ* both by applying an electric displacement field and by electron doping.

Correlated states in moiré materials that emerge by partially filling energetically flattened bands have been intensively explored in hexagonal systems where the low-energy degrees of freedom originate from high-symmetry points such as the K/K' and Γ points of the Brillouin zone [1–5]. A prominent example is magic-angle twisted bilayer graphene where the bands near charge neutrality arise from Dirac cones at the K/K' valleys, leading to an approximate $U(4) \times U(4)$ symmetry in the low-energy sector combining spin, valley, and sublattice degrees of freedom [6]. This system hosts a range of interaction-driven phenomena, including correlated insulators [7], superconductivity [8], and intervalley coherence [9]. Another prominent example are twisted transition metal dichalcogenides (TMDs) such as twisted bilayer 2H WSe₂ and MoTe₂ where strong Ising spin-orbit coupling locks the spin to valley at the K/K' point in the valence band. Here interactions give rise to superconductivity [10–12], itinerant magnetism [13, 14], and the fractional anomalous quantum Hall effect [15, 16]. A parallel line of work has focused on Γ -valley moiré TMDs, where the low-energy bands are valley-less. Examples include the valence band of twisted homobilayers of 2H MoS₂ or 2H MoSe₂ [5] which display correlated states such as Wigner crystals [17], enabled by the flatness of the Γ -valley moiré bands.

It is also possible to have twisted materials with low-energy valleys located at the three inequivalent M points of the hexagonal Brillouin zone [18–21]. Very recently two theoretical groups independently proposed that twisting experimentally exfoliable materials such as SnSe₂ and group 4 TMDs such as ZrS₂ or HfS₂ result in

M -valley moirés [22, 23]. These materials are insulators down to the monolayer with the hexagonal 1T structure and point group D_{3d} , and their conduction band minima generically occurs at the M points [24]. The resulting moiré bands carry a threefold valley degree of freedom and have an approximate spin degeneracy inherited from the monolayer. For sufficiently small twist angles, the dispersion of the lowest moiré bands become negligible, giving rise to an effective $SU(3)$ valley symmetry, which, when combined with spin, yields an emergent $SU(6)$ flavor symmetry.

In this paper, we study the role of electron-electron interactions in the bottommost moiré bands of M -valley moiré systems in the weak-coupling regime, using both aligned and antialigned 1T tSnSe₂ as representative examples. To this end, we use the self-consistent Hartree-Fock method applied to the moiré continuum model that fully takes into account band mixing. In the absence of symmetry breaking, we find that the moiré bands are strongly renormalized by interactions as the electron filling increases from charge neutrality ($\nu = 0$) to full filling ($\nu = 6$) of the low-energy moiré band manifold. In particular, at half filling we find that the bandwidth increases significantly. While this would ordinarily disfavor correlated states, we also find surprisingly that the Van Hove singularity in the density of states gets pinned to the Fermi energy in the presence of interactions which enhances the likelihood of strongly correlated states and superconductivity as observed in other moiré systems such as twisted bilayer graphene near the magic angle.

Mapping the density of states as a function of filling and applied interlayer bias shows a qualitatively differ-

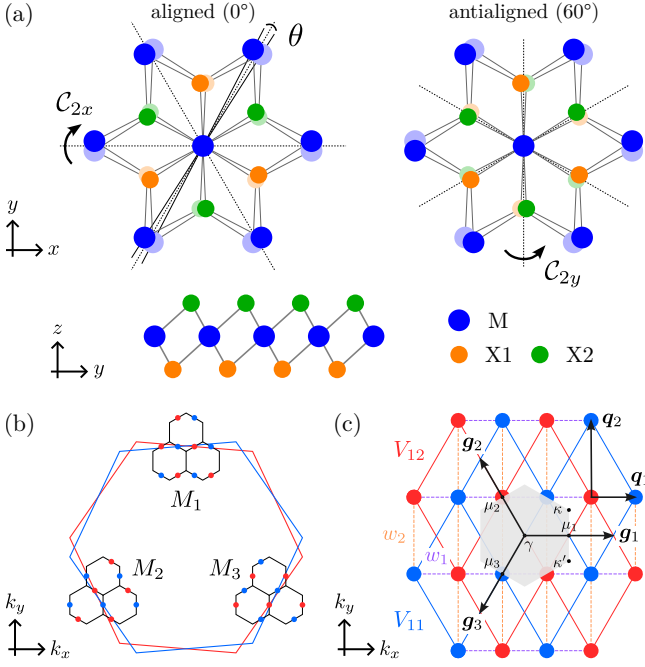


FIG. 1. Real space and momentum space representations for M -valley moiré materials. (a) Lattice structure of twisted aligned and antialigned homobilayer 1T TMDs MX_2 . Here $X1$ ($X2$) is buckled into (out of) the plane, see bottom panel, and the dark and light atoms correspond to layer $l = 1, 2$ which is rotated by $\pm\theta/2$, respectively. Shown for $\theta = 5.09^\circ$ close to the twist center which is chosen here as eclipsing metal atoms. For a general twist center the $D_3 = \langle C_{3z}, C_{2x} \rangle$ symmetry is an approximate emergent symmetry on the moiré scale for $L/a \gg 1$. (b) Brillouin zone of the twisted monolayers (red and blue large hexagons) showing the three M valleys (dots) for both layers and the moiré Brillouin zone (small hexagons). (c) Illustration of the moiré potentials in momentum space for the M_1 valley ($\tau = 1$). Solid (dashed) lines represent intralayer (interlayer) processes and the gray hexagon is the MBZ. Intralayer terms along $\pm\mathbf{g}_1$ are not shown for clarity.

ent behavior for small twist angles near aligned (0°) and antialigned (60°) stacking. Both cases yield a moiré that varies slowly with respect to the atomic scale, but are inequivalent due to the lack of 180° in-plane rotation symmetry of the 1T monolayer. We then study symmetry-broken phases at half filling that spontaneously break time-reversal symmetry and/or rotation symmetry by flavor polarization, but preserve moiré translational symmetry and valley charge conservation. Our study establishes a baseline for correlation effects in M -valley systems, providing a framework for interpreting ongoing and future experimental results on M -valley moiré TMDs.

Model — We consider a twisted homobilayer made from M -valley monolayers with point group D_{3d} . Here layers $l = 1, 2$ are rotated by an angle $\pm\theta/2$, respectively, with respect to aligned (0°) or antialigned (60°) stacking, see Fig. 1(a). In the long-wavelength limit, i.e. for small twist angles, the emergent moiré lattice has period

$L = a/\theta \gg a$ with a the monolayer lattice constant, and emergent point group D_3 generated by C_{3z} and C_{2x} (C_{2y}) for twisting near aligned (antialigned) stacking in the coordinate system of Fig. 1(a).

In particular, we consider semiconductors such as 1T SnSe_2 or 1T ZrS_2 with three spin degenerate conduction band minima at the three M_τ points ($\tau = 1, 2, 3$) [24], illustrated in Fig. 1(b). The corresponding low-energy moiré theory for the conduction band can thus be written as $H = H_0 + H_{ee}$ where $H_0 = \sum_{s=\uparrow,\downarrow} \sum_{\tau=1}^3 H_{s\tau}$ is the single-particle Hamiltonian and H_{ee} is a gate-screened Coulomb interaction. While the twisted bilayer lacks inversion symmetry, an approximate $SU(2)$ symmetry is inherited from the monolayer [22, 23]. Therefore we can write $H_{s\tau} = \int d^2\mathbf{r} \psi_{s\tau}^\dagger \mathcal{H}_\tau \psi_{s\tau}$ with

$$\mathcal{H}_\tau = \begin{bmatrix} \left(\frac{-\hbar^2}{2m_\tau} \right)_{ij} \partial^i \partial^j + V_{\tau 1} & T_\tau^* \\ T_\tau & \left(\frac{-\hbar^2}{2m_\tau} \right)_{ij} \partial^i \partial^j + V_{\tau 2} \end{bmatrix}, \quad (1)$$

where summation over repeated indices is implied, and $\psi_{s\tau} = (\psi_{s\tau 1}, \psi_{s\tau 2})^\top$ are fermion field operators in layer space that satisfy $\{\psi_{s\tau l}^\dagger(\mathbf{r}), \psi_{s'\tau'l'}(\mathbf{r}')\} = \delta_{ss'}\delta_{\tau\tau'}\delta_{ll'}\delta(\mathbf{r}-\mathbf{r}')$. The M points are time-reversal invariant momenta that are related by C_{3z} rotations such that $H_{s,\tau+1} = C_{3z} H_{s\tau} C_{3z}^{-1}$ with $C_{3z} \psi_{s\tau}(\mathbf{r}) C_{3z}^{-1} = \psi_{s,\tau+1}(C_{3z}\mathbf{r})$. Hence the Hamiltonian for each τ is only constrained by time-reversal symmetry, moiré translations, and e.g. for $\tau = 1$ by C_{2x} (C_{2y}) for aligned (antialigned) stacking where we take $M_1 = 2\pi\hat{y}/(\sqrt{3}a)$ for the untwisted bilayer. We thus only specify \mathcal{H}_1 in the following. The monolayer C_{2x} symmetry implies an inverse effective mass tensor $1/m_1 = \text{diag}(m_\perp^{-1}, m_\parallel^{-1})$ and in lowest order, the moiré potentials can be written as

$$V_{1l}(\mathbf{r}) = (-1)^{l+1} \frac{V_z}{2} + \sum_{n=1}^3 2v_{ln} \cos(\mathbf{g}_n \cdot \mathbf{r} + \psi_{ln}), \quad (2)$$

$$T_1(\mathbf{r}) = T_1^*(\mathbf{r}) = \sum_{n=1}^2 2w_n \cos(\mathbf{q}_n \cdot \mathbf{r} + \phi_n), \quad (3)$$

where V_z is an interlayer bias due to an external electric field perpendicular to the layers, which breaks the out-of-plane twofold rotation symmetry. Here the \mathbf{g}_n are the shortest nonzero moiré reciprocal vectors related by C_{3z} with $\mathbf{g}_1 = 4\pi\hat{x}/(\sqrt{3}L)$, $\mathbf{q}_1 = \mathbf{g}_1/2$, and $\mathbf{q}_2 = \mathbf{q}_1 + \mathbf{g}_2$. These correspond to the dominant intralayer and interlayer moiré scattering processes, respectively. We can understand this intuitively from the geometry of the moiré Brillouin zone (MBZ) in a given M valley, as shown in Fig. 1(c). Twofold rotation symmetry further requires that $v_{21} = v_{11}$, $v_{22} = v_{13}$, and $v_{23} = v_{12}$. In addition, $\psi_{21} = \pm\psi_{11}$, $\psi_{22} = \pm\psi_{13}$, and $\psi_{23} = \pm\psi_{12}$, for aligned (C_{2x}) and antialigned (C_{2y}) stacking, respectively. For the interlayer tunneling, we further have $\phi_2 = 0$ for aligned stacking and $\phi_1 = 0$ for antialigned stacking. See Supplemental Material (SM) [25] for details.

Furthermore, in the local-stacking approximation [26], the inversion ($\mathbf{r} \mapsto -\mathbf{r}$ and $z \mapsto -z$) and mirror ($z \mapsto -z$) symmetry of untwisted aligned and antialigned bilayers implies $V_{\tau 1}(\mathbf{r}) = V_{\tau 2}(\pm \mathbf{r})$, respectively [22, 23]. In this case, the theory for $V_z = 0$ has additional intravalley model symmetries, given respectively by mirror $\mathcal{M}_z \psi_{s\tau}(\mathbf{r}) \mathcal{M}_z^{-1} = \sigma_x \psi_{s\tau}(\mathbf{r})$ and inversion $\mathcal{P} \psi_{s\tau}(\mathbf{r}) \mathcal{P}^{-1} = \sigma_x \psi_{s\tau}(-\mathbf{r})$. The latter results in $T_\tau(\mathbf{r}) = T_\tau(-\mathbf{r})$ for antialigned stacking. Incidentally, we notice a previously unreported duality between these approximate moiré symmetries inherited from untwisted bilayers, for aligned (antialigned) 1T tTMDs such as tSnSe₂ and tZrS₂ with monolayer point group D_{3d} , and antialigned (aligned) 2H tTMDs such as tWSe₂ and tMoTe₂ with monolayer point group D_{3h} . This immediately implies that antialigned 1TtTMDs contain two degenerate low-energy stacking configurations in the moiré cell and relax towards a triangular soliton network of partial shear dislocations, while aligned 1TtTMDs only have one low-energy configuration resulting in a honeycomb network of full shear dislocations [27].

We note that for the choice of basis used to write Eq. (1) the tunneling is not moiré periodic: $T_1(\mathbf{r} + \mathbf{L}) = (-1)^m T_1(\mathbf{r})$ with $\mathbf{g}_1 \cdot \mathbf{L} = 2\pi m$ and integer m . The advantage of this basis is that symmetries act locally in momentum space, because we gauged the momentum of the rotated M_τ points of layer l denoted as $\mu_{\tau l}$. On the other hand, because \mathcal{H}_τ is only quasiperiodic in this basis, it obfuscates the fact that for aligned stacking, the local-stacking symmetry \mathcal{M}_z is nonsymmorphic in momentum space because it exchanges $\mu_{\tau 1}$ and $\mu_{\tau 2}$ which are separated by *half* a reciprocal lattice vector [23]. Consequently, \mathcal{M}_z does not commute with certain moiré translations, e.g. \mathbf{L}_1 for $\tau = 1$ with $\mathbf{g}_1 \cdot \mathbf{L}_1 = 2\pi$ [23]. Hence, for each valley the \mathcal{M}_z eigenbasis realizes a projective representation of the translation group equivalent to threading half a flux quantum (which is time-reversal invariant). In the \mathcal{M}_z eigenbasis, the moiré cell is doubled yielding two orbitals with opposite mirror eigenvalues for the low-energy moiré bands [23].

To diagonalize H_0 by Fourier transform, we restore the origin by letting $\psi_{s\tau l} \rightarrow e^{-i\mu_{\tau l} \cdot \mathbf{r}} \psi_{s\tau l}$ such that $T_1(\mathbf{r}) \rightarrow e^{-i\mathbf{g}_1 \cdot \mathbf{r}/2} T_1(\mathbf{r})$. This yields Bloch eigenstates $|\phi_{\tau n \mathbf{k}}^{(l)}\rangle = \sum_{\mathbf{g}} u_{\tau n \mathbf{k}}^{(l)}(\mathbf{g}) |\mathbf{k} + \mathbf{g}\rangle$ with energies $\varepsilon_{\tau n \mathbf{k}} = \varepsilon_{\tau+1, n, \mathcal{C}_3 z \mathbf{k}}$ where τ is defined modulo 3. The model in Eq. (1) and the moiré potentials from Eqs. (2) and (3) were previously constructed and studied in Refs. [22, 23] at charge neutrality in the absence of an interlayer bias V_z . In what follows we use parameters for tSnSe₂ fitted to density-functional theory (DFT) [23] and which are listed in the SM [25]. Here we have chosen parameters that reproduce well the low-energy moiré bands at charge neutrality obtained from DFT. For aligned stacking, these parameters obey the local-stacking approximation, while for antialigned stacking, this is only approximately true.

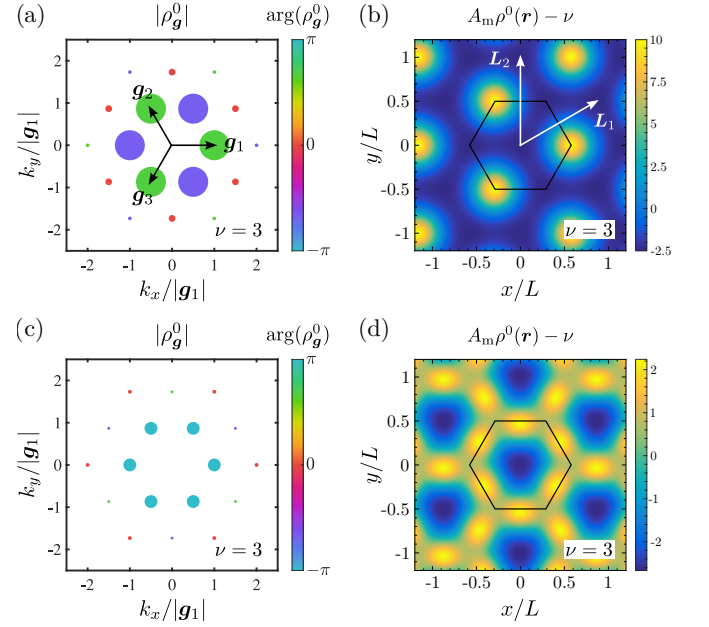


FIG. 2. Large moiré scale density fluctuations in the noninteracting model highlight the importance of Coulomb interactions. (a) Density fluctuations for aligned 3.89° 1T tSnSe₂ at half filling of the low-energy moiré bands ($\nu = 3$) in the absence of electron-electron interactions. The size gives the magnitude $|\rho_g^0|$ and the color its phase $\arg(\rho_g^0)$. (b) Corresponding density $\rho^0(\mathbf{r})$ showing only the fluctuations in units of $A_m^{-1} = 2/(\sqrt{3}L^2)$, and where the hexagon is the moiré cell. The large amplitude on the moiré scale gives a strong Hartree potential. The density respects D_3 because we sum over all three M valleys. (c) Density fluctuations for antialigned stacking using the same twist angle and scale as in (a). (d) Same as (b) for antialigned stacking. In this case, the density fluctuations are much smaller as compared to aligned stacking for the same twist, giving a weaker Hartree effect. Because the density for each M valley is related by \mathcal{C}_{3z} symmetry, they roughly coincide for aligned stacking, forming a triangular lattice with three orbitals at each site [23]. On the other hand, for antialigned stacking, we see that each of the three valleys is localized on one sublattice of a kagome lattice.

Interaction-renormalized moiré bands — We now investigate the effect of electron-electron interactions on the low-energy M -valley moiré bands using the self-consistent Hartree-Fock (HF) approximation implemented in band basis [25, 28]. In particular, we consider a dual-gate screened Coulomb interaction $U_{\mathbf{q}} = e^2 \tanh(qd)/(2\epsilon\epsilon_0 q)$ where d is the gate-to-sample distance. Throughout this work, we set $d = 20$ nm and treat the relative dielectric constant ϵ of the dielectric spacer as a phenomenological parameter that tunes the interaction strength. We anticipate that $\epsilon \approx 25$ corresponds to the physically relevant scenario since this value reproduces experimental features for other TMD moiré systems e.g. 2H-tWSe₂ [13, 29].

To illustrate the effect of interactions in the weak-coupling regime, we first consider the Hartree contri-

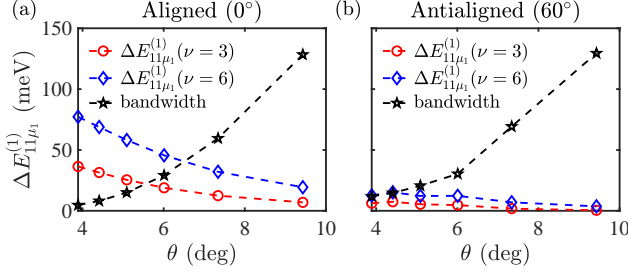


FIG. 3. Comparison of one-shot Hartree correction and bandwidth as a function of twist angle for (a) aligned and (b) antialigned 1T tSnSe₂. Figures use $\epsilon = 25$, $V_z = 0$, and valley $\tau = 1$ at the μ_1 point of the MBZ for $\nu = 3$ and $\nu = 6$.

bution written as $H_H = \sum_{s,\tau,\mathbf{k}} \sum_{\mathbf{g} \neq 0} \rho_{\mathbf{g}} U_{\mathbf{g}} c_{s\tau,\mathbf{k}+\mathbf{g}}^\dagger c_{s\tau,\mathbf{k}}$ where this mean-field electrostatic interaction depends on the carrier density fluctuations given by

$$\rho_{\mathbf{g}} = \frac{2}{N_m A_m} \sum_{\tau,n,\mathbf{k} \in \text{occ}} \sum_{\mathbf{g}',l} \left[u_{\tau n \mathbf{k}}^{(l)}(\mathbf{g}') \right]^* u_{\tau n \mathbf{k}}^{(l)}(\mathbf{g} + \mathbf{g}'). \quad (4)$$

Here the factor 2 accounts for spin, A_m the moiré cell area, N_m the number of cells, i.e. the number of \mathbf{k} points in our grid, n is the band index, and $u_{\tau n \mathbf{k}}^{(l)}(\mathbf{g})$ are Fourier amplitudes of the eigenstates of the mean-field Hamiltonian. We show $\rho_{\mathbf{g}}$ in the absence of interactions in Fig. 2(a) for aligned 1T tSnSe₂ with $\theta = 3.89^\circ$ at half filling of the low-energy moiré band manifold ($\nu = 3$). We find that the density fluctuations have significant support only on the first three reciprocal stars with the dominant contribution coming from the first star. They also obey $D_3 = \langle C_{3z}, C_{2x} \rangle$ symmetry because all three M valleys are equally filled in the noninteracting case. In particular, the first star is not constrained by C_{2x} and is generally complex. In real space, the density is strongly localized on a triangular lattice and on the order of $10A_m^{-1}$, see Fig. 2(b). Because the M valleys are related by C_{3z} one obtain a triangular lattice with three orbitals corresponding to the valleys [23]. On the other hand, for antialigned stacking, the density fluctuations are much weaker, as shown in Fig. 2(c). Moreover, now $D_3 = \langle C_{3z}, C_{2y} \rangle$ makes the first star real, such that the density has approximate C_{6z} symmetry, as can be seen in Fig. 2(d). One obtains a kagome lattice with each M valley localized on one sublattice [30]. To further illustrate the Hartree effect, we plot the one-shot Hartree shift $\Delta E_{\tau n \mathbf{k}}^{(1)} = \sum_{\mathbf{g} \neq 0} \rho_{\mathbf{g}} U_{\mathbf{g}} \Lambda_{\tau n \mathbf{k}}(\mathbf{g})$ of the bottom band for $\tau = 1$ at the μ_1 point of the moiré Brillouin zone as a function of twist angle in Fig. 3 for both aligned and antialigned stacking. Here we define the form factor $\Lambda_{\tau n \mathbf{k}}(\mathbf{g}) = \sum_{l,\mathbf{g}'} [u_{\tau n \mathbf{k}}^{(l)}(\mathbf{g}')]^* u_{\tau n \mathbf{k}}^{(l)}(\mathbf{g}' + \mathbf{g})$. Similarly to twisted bilayer graphene near the magic angle, strong density modulations on the moiré scale yield a significant Hartree effect (see e.g. Ref. [31], and references therein). By contrast the Hartree potential can often be neglected

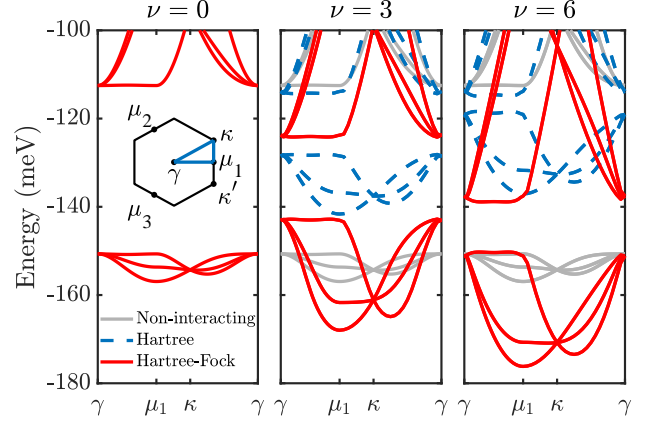


FIG. 4. Hartree-Fock bands for $\epsilon = 25$ of the symmetry unbroken state for *aligned* 3.89° 1T tSnSe₂ with interlayer bias $V_z = 30$ meV, shown for filling factors $\nu = 0, 3$, and 6 . A finite V_z splits the bands of the three valleys which are otherwise pairwise degenerate along the chosen path. At $\nu = 0$ (left panel) the net density vanishes and the bands are those fitted to DFT, giving three low-energy bands, one for each valley [23]. As the filling increases (middle and right panels) Hartree and Fock corrections widen the low-energy band manifold and reduce the gap to the high-energy dispersive bands.

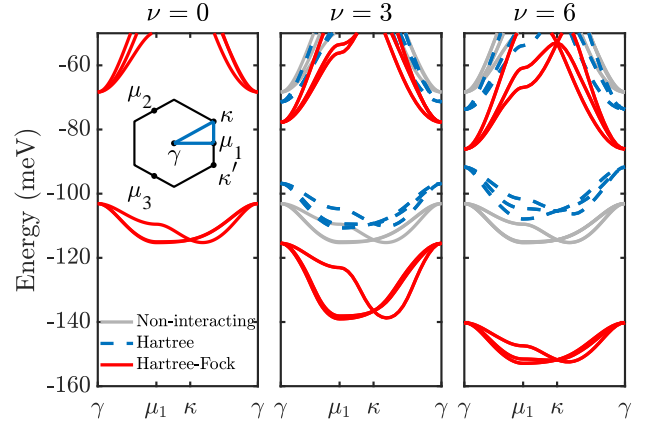


FIG. 5. HF bands for $\epsilon = 25$ of the symmetry unbroken state for *antialigned* 3.89° 1T tSnSe₂ with $V_z = 30$ meV, shown for filling factors $\nu = 0, 3$, and 6 . A finite V_z splits the bands of the three valleys which are otherwise pairwise degenerate along the shown path. At $\nu = 0$ (left panel) the net density vanishes and the bands are those fitted to DFT, giving three low-energy bands, one for each valley [23]. As the filling increases (middle and right panels) HF corrections increase the gap to remote bands, and initially increase the bandwidth ($\nu = 3$) but leave it unchanged for larger filling ($\nu = 6$).

for K valley tTMDs such as aligned 2H-tWSe₂ (see e.g. Ref. [29], and references therein).

Having established that M -valley moiré bands feature a significant Hartree potential, we now consider the symmetry unbroken HF state. This state serves as a *parent*

state from which symmetry-broken ground states may emerge. While the symmetry unbroken state is generally not the HF ground state, it is a local energy minimum of the mean field Hamiltonian. We find that both Hartree and Fock contributions play a dominant role in band renormalization. In Fig. 4, we show the HF band structures for aligned 1T tSnSe₂ with $\theta = 3.89^\circ$ at filling factors $\nu = 0, 3$, and 6. At charge neutrality ($\nu = 0$) the bands are given by H_0 obtained from the fit to DFT, featuring an isolated and flattened low-energy manifold. As electrons are added, the Hartree term increases the bandwidth and reduces the gap between the lowest and remote bands, while the Fock term tends to enhance both the bandwidth and gap. These effects compete, resulting in a non-monotonic band evolution with filling. Similarly, for antialigned stacking, shown in Fig. 5 the HF corrections strongly modify the low-energy moiré bands. Though in this case, the bandwidth first increases with filling then saturates as one approaches full filling.

The interaction-renormalized moiré bands are further illustrated in Fig. 6, which shows the density of states (DOS) as a function of interlayer bias V_z and filling factor ν . We show the DOS for both the noninteracting (left) and HF (right) case, for both aligned (top) and antialigned (bottom) stacking, using parameters for 3.89° tSnSe₂. The DOS is symmetric in V_z because V_z is odd under twofold out-of-plane rotation symmetry of the moiré. In the absence of interactions and $V_z = 0$, there is a Van Hove singularity (VHS) close to charge neutrality ($\nu = 0$) for aligned stacking due to two saddle points in the lowest moiré band at $k_x = 0$ and $k_y = \pm\pi/L$ for $\tau = 1$. As $|V_z|$ increases, the saddle points merge with a minimum, giving rise to a high-order VHS [32] at a critical value of V_z . The resulting saddle point then becomes pinned at $\mu_{\tau 1}$ or $\mu_{\tau 2}$ depending on the sign of V_z . Another VHS exists close to full filling where the band is flattened ($\nu = 6$).

On the other hand, for antialigned stacking, there is a VHS close to half filling ($\nu = 3$) for $V_z = 0$ due to saddle points in the dispersion at the $\mu_{\tau l}$ points, which are split in energy at finite V_z . Accordingly, the VHS moves from half filling to charge neutrality as $|V_z|$ increases, see bottom left panel of Fig. 6. We also note that in a given valley, the moiré bands for aligned stacking are quasi one-dimensional (1D) near zero interlayer bias, but become increasingly 2D as $|V_z|$ increases. Remarkably, the opposite is true for antialigned stacking. This implies that the quasi 1D nature of the M -valley moiré bands can be tuned *in situ* with an applied electric field perpendicular to the twisted layers. This is illustrated in Fig. 7 where we show the energy contours of the lowest-energy moiré band of valley $\tau = 1$ for several V_z .

When interactions are included, the DOS is significantly modified. The Hartree and Fock terms change the dispersion of the VHS in the $\nu - V_z$ plane from “V shaped” to “Y shaped” which results from pinning of the

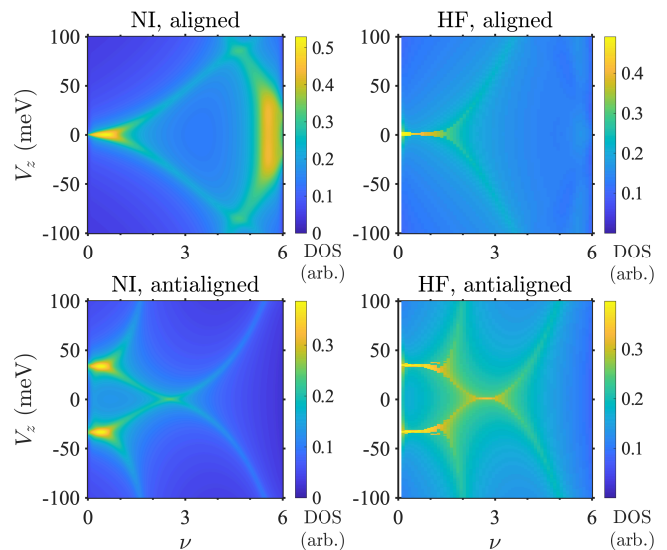


FIG. 6. Density of states (DOS) of the noninteracting (left) and *symmetry unbroken* Hartree-Fock state (right) as a function of filling factor ν (number of electrons per moiré cell) and interlayer bias V_z due to an applied electric displacement field. We consider 3.89° 1T tSnSe₂ for both aligned (top) and antialigned (bottom) stacking. In the noninteracting case, the DOS for $V_z = 0$ shows Van Hove singularities (VHSs) near the band edges for aligned stacking and just below half filling for antialigned stacking, that disperse in the $\nu - V_z$ plane. Interestingly, for antialigned stacking the VHS moves towards charge neutrality as $|V_z|$ increases. Interactions modify this picture: HF corrections soften the Lifshitz transition and removes the VHS near full filling for aligned stacking. Moreover, the VHSs become pinned to the Fermi energy near charge neutrality, and also near half filling for antialigned stacking which give rise to the “Y shaped” features.

Fermi energy to the VHS. This phenomenon also occurs in Hubbard models [33], kagome metals [34], and twisted bilayer graphene [31, 35]. Here we find that the VHS pinning is driven by the Fock term which favors a simply-connected Fermi pocket pushing the VHS to the Fermi surface [36]. In addition, the peaks broaden such that the Lifshitz transition is washed out in the DOS. Moreover, for aligned stacking, the secondary VHS near full filling is strongly suppressed by the Hartree term which broadens the band.

While we have only considered a single twist angle in this section, we find that the density of states is qualitatively similar for twist angles $\lesssim 5^\circ$ for which the moiré effect is strong. For larger twist angles, the distinction between aligned and antialigned stacking is reduced and the moiré potentials are weaker compared to the kinetic energy scale set by the twist angle. This is evident from the Lifshitz transition $\nu \propto |V_z|$ between layer-polarized and layer-hybridized regimes, as shown in the SM [25].

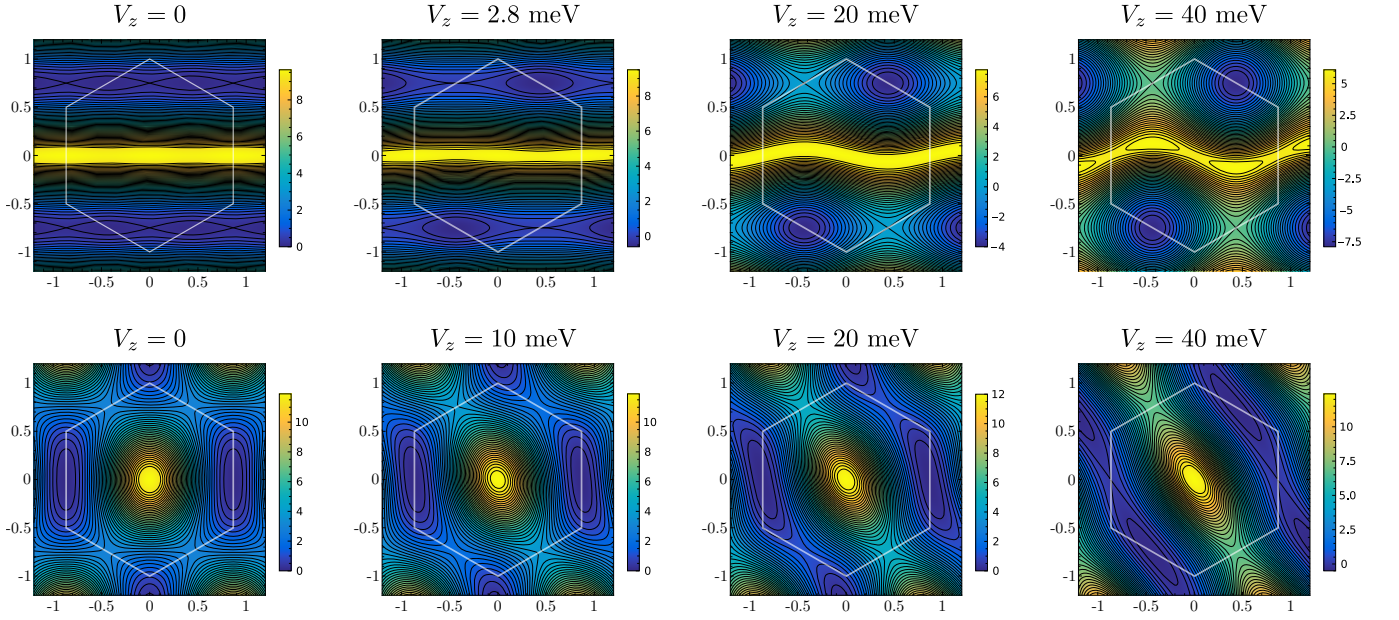


FIG. 7. Energy dispersion of the lowest-energy $\tau = 1$ moiré band for aligned (top row) and antialigned (bottom row) stacking of 3.89° 1T tSnSe₂ for several V_z as indicated. For aligned (antialigned) stacking, the energy zero is set at the low-energy Van Hove singularity (μ_1 point of the MBZ). As we increase V_z , two low-energy saddle points merge with a minimum resulting in contours that touch tangentially for $V_z \approx 2.8$ meV, giving rise to a high-order VHS. Moreover, the band evolves from quasi-1D to 2D, as a finite V_z breaks \mathcal{M}_z symmetry [23] and one eventually recovers two decoupled layers. On the other hand, for antialigned stacking the VHS at half filling for $V_z = 0$ moves towards charge neutrality as we increase $|V_z|$. Simultaneously the band evolves from 2D to quasi-1D in an intermediate V_z window.

Correlated insulator at half-filling — Finally, we consider the symmetry-broken correlated insulator at half filling ($\nu = 3$) of the low-energy moiré bands. To describe these correlated states, it is convenient to introduce the single-particle density matrix $\hat{\rho}(\mathbf{k}) = \langle c_{s\tau, \mathbf{k}}^\dagger c_{s\tau, \mathbf{k}} \rangle$. Different Hartree–Fock symmetry-broken ansatzes correspond to different choices of $\hat{\rho}(\mathbf{k})$, subject to the constraints $(1/N_m) \sum_{\mathbf{k}} \text{Tr}[\hat{\rho}(\mathbf{k})] = \nu$ and $\hat{\rho}^2(\mathbf{k}) = \hat{\rho}(\mathbf{k})$ which enforce charge conservation and the Pauli principle. For simplicity, and to illustrate the general principles, we consider only states that conserve valley charge and moiré translational symmetry. In this case, $\hat{\rho}(\mathbf{k})$ is diagonal in valley and moiré periodic. Moreover, we can take it diagonal in spin because of the (approximate) spin SU(2) symmetry of the noninteracting theory. Our analysis excludes, for example, possible intervalley-coherent order, or charge density waves and layer ferromagnets (that break \mathcal{M}_z) which as discussed earlier requires broken moiré translational symmetry. At half filling, under these assumptions, there are two HF *ansatzes* yielding phases that spontaneously break time-reversal symmetry: (1) a fully spin-polarized state ($S = 3/2$) that equally populates the three M valleys and thus preserves \mathcal{C}_{3z} rotation symmetry, and (2) a partially spin-polarized ($S = 1/2$) nematic state which breaks \mathcal{C}_{3z} . As shown in Fig. 8(a), for aligned stacking the nematic state is favored for stronger interactions (smaller ϵ). For weaker interactions, the isotropic state is favored but the energy difference is only several

meV. For antialigned stacking, shown in Fig. 8(b), the isotropic state is the ground state with a transition to a gapless nematic state as the interaction strength is reduced and V_z increases. The latter may be identified experimentally from the anisotropic conductivity $\sigma_{xx} - \sigma_{yy}$ or $\sigma_{xy} + \sigma_{yx}$ which are nonzero only in the absence of \mathcal{C}_{3z} symmetry. In both cases, the magnitude of the correlated gap depends weakly on the interlayer bias. As expected, it decreases when the ratio between the bandwidth, which is controlled by twist angle and V_z (see Fig. 3), and the interaction strength, controlled by ϵ , increases. For larger twist angles, the gap closes yielding a partially spin-polarized (nearly) isotropic metal. This is shown in Fig. 8(c) and (d) for twisting near aligned and antialigned stacking, respectively.

Conclusions — The possibility of experimentally exfoliable M -valley moiré systems in 1T twisted transition metal dichalcogenide homobilayers (tTMDs) fundamentally expands the landscape of correlated electron physics beyond the well-explored K/K' and Γ valley platforms. In particular, our demonstration that Van Hove singularities in 1T tTMDs can be pinned to the Fermi energy by electrostatic doping and external electric displacement fields opens up new pathways for engineering unconventional superconductivity and quantum criticality in van der Waals heterostructures.

We have also shown that one can *in situ* tune 1T tTMDs, using just electric fields, between quasi-1D and

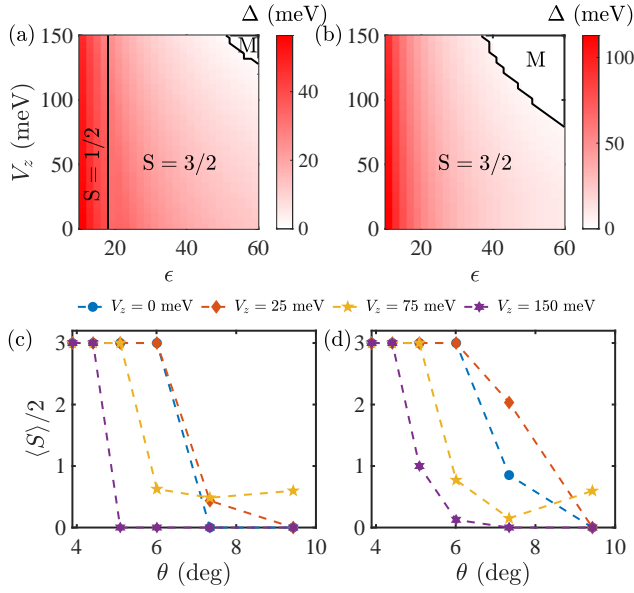


FIG. 8. (top) Interaction-induced correlated gap Δ at half filling as a function of interlayer bias V_z and dielectric constant ϵ for (a) aligned stacking and (b) antialigned stacking. The gap decreases with increasing ϵ due to enhanced screening, and shows only a weak dependence on V_z . (bottom) Spin expectation value of the ground state per particle in units of \hbar for (c) aligned and (d) antialigned stacking as a function of twist angle θ for several V_z . As θ increases, the correlated gap closes and the system becomes a partially spin-polarized metal.

2D regimes within the same device. This creates unprecedented opportunities to study dimensional crossovers in strongly correlated systems, an important question in condensed matter physics that is often difficult to study experimentally. Moreover, control over three valleys yield a potentially much richer phase diagram than two (K/K') or one (Γ) valley materials and with analogs to high-energy physics where the M valleys take on the role of a “color” charge. This follows from the decomposition: $U(2) \times U(2) \times U(2) \simeq U(1) \times SU(2) \times SU(3)$. While we restricted ourselves here to spin and valley polarized ground states that conserve the two valley charges, because the band dispersion breaks $SU(3)$ explicitly there are a plethora of potential intervalley-coherent ground states parameterized by the Gell-Mann matrices. Moreover, fluctuations from a nascent intervalley coherent state may serve as a pairing glue for superconductivity, similar to kagome metals [37]. Furthermore, the role of external heterostrain, which explicitly breaks C_{3z} symmetry, acting as an external field for the three M valleys remains to be explored in this novel moiré system. This six-flavor (spin and valley) structure combined with quasi-1D channels within each valley creates opportunities for hybrid quantum phases that couple distinct many-body tendencies. We anticipate correlation-driven transitions, electrically tunable quantum criticality, and designer su-

perconducting states with controllable gap symmetries. Unlike existing moiré systems where such control often requires precise angle tuning, our work shows that M -valley materials offer robust gate-voltage control over electronic correlations, promising more practical routes for designer quantum phases.

Acknowledgments — We thank Daniel Bennett for helpful discussions and for collaboration on another related project. Computation was done on Stampede3 at the Texas Advanced Computing Center through allocation PHY240263 from the ACCESS program supported by the U.S. National Science Foundation. L.P. and S.A. are supported by a start-up grant at Washington University in St. Louis. C.D.B. and E.J.M. are supported by the U.S. Department of Energy under Grant No. DE-FG02-84ER45118.

Note Added — After completion of this work, we became aware of arXiv:2508.10098v1, which also examines the role of interactions in M -valley TMDs. In contrast to our work, this study constructs Wannier orbital models to analyze the strong-coupling limit, while our work focuses on the weak-coupling limit using self-consistent Hartree-Fock. Together, these complementary approaches highlight the importance of interactions across different regimes in M -valley moiré systems.

-
- [1] J. M. B. Lopes dos Santos, N. M. R. Peres, and A. H. Castro Neto, Graphene Bilayer with a Twist: Electronic Structure, *Physical Review Letters* **99**, 256802 (2007).
 - [2] E. Suárez Morell, J. D. Correa, P. Vargas, M. Pacheco, and Z. Barticevic, Flat bands in slightly twisted bilayer graphene: Tight-binding calculations, *Physical Review B* **82**, 121407 (2010).
 - [3] R. Bistritzer and A. H. MacDonald, Moiré bands in twisted double-layer graphene, *Proceedings of the National Academy of Sciences* **108**, 12233 (2011).
 - [4] F. Wu, T. Lovorn, E. Tutuc, I. Martin, and A. MacDonald, Topological Insulators in Twisted Transition Metal Dichalcogenide Homobilayers, *Physical Review Letters* **122**, 086402 (2019).
 - [5] M. Angeli and A. H. MacDonald, Gamma valley transition metal dichalcogenide moiré bands, *Proceedings of the National Academy of Sciences* **118**, e2021826118 (2021).
 - [6] N. Bultinck, E. Khalaf, S. Liu, S. Chatterjee, A. Vishwanath, and M. P. Zaletel, Ground State and Hidden Symmetry of Magic-Angle Graphene at Even Integer Filling, *Physical Review X* **10**, 031034 (2020).
 - [7] Y. Cao, V. Fatemi, A. Demir, S. Fang, S. L. Tomarken, J. Y. Luo, J. D. Sanchez-Yamagishi, K. Watanabe, T. Taniguchi, E. Kaxiras, R. C. Ashoori, and P. Jarillo-Herrero, Correlated insulator behaviour at half-filling in magic-angle graphene superlattices, *Nature* **556**, 80 (2018).
 - [8] Y. Cao, V. Fatemi, S. Fang, K. Watanabe, T. Taniguchi, E. Kaxiras, and P. Jarillo-Herrero, Unconventional superconductivity in magic-angle graphene superlattices, *Nature* **584**, 77 (2020).

- ture **556**, 43 (2018).
- [9] K. P. Nuckolls, R. L. Lee, M. Oh, D. Wong, T. Soejima, J. P. Hong, D. Călugăru, J. Herzog-Arbeitman, B. A. Bernevig, K. Watanabe, T. Taniguchi, N. Regnault, M. P. Zaletel, and A. Yazdani, Quantum textures of the many-body wavefunctions in magic-angle graphene, *Nature* **620**, 525 (2023).
 - [10] Y. Xia, Z. Han, K. Watanabe, T. Taniguchi, J. Shan, and K. F. Mak, Superconductivity in twisted bilayer WSe₂, *Nature* **637**, 833 (2025).
 - [11] Y. Guo, J. Pack, J. Swann, L. Holtzman, M. Cothrine, K. Watanabe, T. Taniguchi, D. G. Mandrus, K. Barmak, J. Hone, A. J. Millis, A. Pasupathy, and C. R. Dean, Superconductivity in 5.0° twisted bilayer WSe₂, *Nature* **637**, 839 (2025).
 - [12] F. Xu, Z. Sun, J. Li, C. Zheng, C. Xu, J. Gao, T. Jia, K. Watanabe, T. Taniguchi, B. Tong, L. Lu, J. Jia, Z. Shi, S. Jiang, Y. Zhang, Y. Zhang, S. Lei, X. Liu, and T. Li, Signatures of unconventional superconductivity near reentrant and fractional quantum anomalous Hall insulators (2025), arXiv:2504.06972.
 - [13] P. Knüppel, J. Zhu, Y. Xia, Z. Xia, Z. Han, Y. Zeng, K. Watanabe, T. Taniguchi, J. Shan, and K. F. Mak, Correlated states controlled by a tunable van Hove singularity in moiré WSe₂ bilayers, *Nature Communications* **16**, 1959 (2025).
 - [14] A. Ghiotto, L. Wei, L. Song, J. Zang, A. B. Tazi, D. Ostrom, K. Watanabe, T. Taniguchi, J. C. Hone, D. A. Rhodes, A. J. Millis, C. R. Dean, L. Wang, and A. N. Pasupathy, Stoner instabilities and Ising excitonic states in twisted transition metal dichalcogenides (2024), arXiv:2405.17316.
 - [15] Y. Zeng, Z. Xia, K. Kang, J. Zhu, P. Knüppel, C. Vaswani, K. Watanabe, T. Taniguchi, K. F. Mak, and J. Shan, Thermodynamic evidence of fractional Chern insulator in moiré MoTe₂, *Nature* **622**, 69 (2023).
 - [16] H. Park, J. Cai, E. Anderson, Y. Zhang, J. Zhu, X. Liu, C. Wang, W. Holtzmann, C. Hu, Z. Liu, T. Taniguchi, K. Watanabe, J.-H. Chu, T. Cao, L. Fu, W. Yao, C.-Z. Chang, D. Cobden, D. Xiao, and X. Xu, Observation of fractionally quantized anomalous Hall effect, *Nature* **622**, 74 (2023).
 - [17] N. Kaushal, N. Morales-Durán, A. H. MacDonald, and E. Dagotto, Magnetic ground states of honeycomb lattice Wigner crystals, *Communications Physics* **5**, 289 (2022).
 - [18] T. Kariyado and A. Vishwanath, Flat band in twisted bilayer Bravais lattices, *Physical Review Research* **1**, 033076 (2019).
 - [19] M. Fujimoto, T. Kawakami, and M. Koshino, Perfect one-dimensional interface states in a twisted stack of three-dimensional topological insulators, *Physical Review Research* **4**, 043209 (2022).
 - [20] T. Kariyado, Twisted bilayer BC₃: Valley interlocked anisotropic flat bands, *Physical Review B* **107**, 085127 (2023).
 - [21] K. Bao, H. Wang, Z. Liu, and J. Wang, Anisotropic moiré band flattening in twisted bilayers of M-valley MXenes, *Physical Review B* **112**, L041406 (2025).
 - [22] C. Lei, P. T. Mahon, and A. H. MacDonald, Moiré band theory for M-valley twisted transition metal dichalcogenides (2024), arXiv:2411.18828.
 - [23] D. Călugăru, Y. Jiang, H. Hu, H. Pi, J. Yu, M. G. Vergniory, J. Shan, C. Felser, L. M. Schoop, D. K. Efetov, K. F. Mak, and B. A. Bernevig, Moiré materials based on M-point twisting, *Nature* **643**, 376 (2025).
 - [24] Q. Zhao, Y. Guo, K. Si, Z. Ren, J. Bai, and X. Xu, Elastic, electronic, and dielectric properties of bulk and monolayer ZrS₂, ZrSe₂, HfS₂, HfSe₂ from van der Waals density-functional theory, *physica status solidi (b)* **254**, 1700033 (2017).
 - [25] See Supplemental Material at [insert link] for a derivation of the moiré continuum Hamiltonian from symmetry.
 - [26] J. Jung, A. M. DaSilva, A. H. MacDonald, and S. Adam, Origin of band gaps in graphene on hexagonal boron nitride, *Nature Communications* **6**, 6308 (2015).
 - [27] C. De Beule, G. N. Pallewela, M. M. A. Ezzi, L. Peng, E. J. Mele, and S. Adam, Theory for Lattice Relaxation in Marginal Twist Moirés (2025), arXiv:2503.19162.
 - [28] L. Peng, G. Vignale, and S. Adam, Many-body perturbation theory for moiré systems (2025), arXiv:2502.06968.
 - [29] L. Peng, C. D. Beule, D. Li, L. Yang, E. J. Mele, and S. Adam, Magnetism in Twisted Bilayer WSe₂ (2025), arXiv:2503.09689.
 - [30] B. A. Bernevig, Talk at “Quantum Designer’s Special Edition: 100 Years of Quantum (QD100)”, Miramar Palace, Donostia-San Sebastián, Spain (2025).
 - [31] M. M. A. Ezzi, L. Peng, Z. Liu, J. H. Z. Chao, G. N. Pallewela, D. Foo, and S. Adam, A self-consistent Hartree theory for lattice-relaxed magic-angle twisted bilayer graphene (2024), arXiv:2404.17638.
 - [32] N. F. Q. Yuan, H. Isobe, and L. Fu, Magic of high-order van Hove singularity, *Nature Communications* **10**, 5769 (2019).
 - [33] V. Y. Irkhin, A. A. Katanin, and M. I. Katsnelson, Robustness of the Van Hove Scenario for High- T_c Superconductors, *Physical Review Letters* **89**, 076401 (2002).
 - [34] P. K. Nag, R. Batabyal, J. Ingham, N. Morali, H. Tan, J. Koo, A. Consiglio, E. Liu, N. Avraham, R. Queiroz, R. Thomale, B. Yan, C. Felser, and H. Beidenkopf, Pomeranchuk Instability Induced by an Emergent Higher-Order van Hove Singularity on the Distorted Kagome Surface of Co₃Sn₂S₈ (2024), arXiv:2410.01994.
 - [35] T. Cea, N. R. Walet, and F. Guinea, Electronic band structure and pinning of Fermi energy to Van Hove singularities in twisted bilayer graphene: A self-consistent approach, *Physical Review B* **100**, 205113 (2019).
 - [36] C. Huang, T. M. R. Wolf, W. Qin, N. Wei, I. V. Blinov, and A. H. MacDonald, Spin and orbital metallic magnetism in rhombohedral trilayer graphene, *Physical Review B* **107**, L121405 (2023).
 - [37] S. Zhou and Z. Wang, Chern Fermi pocket, topological pair density wave, and charge-4e and charge-6e superconductivity in kagomé superconductors, *Nature Communications* **13**, 7288 (2022).
 - [38] V. M. Galitskii and A. B. Migdal, Application of Quantum Field Theory Methods to the Many Body Problem, *JETP* **7**, 96 (1958).

Supplemental Material for “Role of electron-electron interactions in M -valley twisted transition metal dichalcogenides”

CONTENTS

First-order Hartree energy shift	S1
Angle-dependent fitting parameters of the continuum model	S1
Hartree-Fock Theory	S1
Density of states for additional twist angles	S3

S1. FIRST-ORDER HARTREE ENERGY SHIFT

We estimate the energy correction due to the Hartree potential using first-order perturbation theory. The Hartree potential takes the form

$$H_H = \sum_{s,\tau,\mathbf{k}} \sum_{\mathbf{g} \neq 0} \rho_{\mathbf{g}} U_{\mathbf{g}} c_{s\tau,\mathbf{k}+\mathbf{g}}^\dagger c_{s\tau,\mathbf{k}}, \quad (\text{S1})$$

where $\rho_{\mathbf{g}}$ is the electronic density in reciprocal space and $U_{\mathbf{g}}$ is the Fourier component of the Coulomb interaction, given in 2D by $U_{\mathbf{q}} = e^2 \tanh(qd)/(2\epsilon\epsilon_0 q)$ where d is the gate-to-sample distance.

To compute the energy shift to a Bloch eigenstate $|\psi_{\tau n \mathbf{k}}\rangle$, we evaluate the expectation value of H_H in that state

$$\Delta E_{\tau n \mathbf{k}}^{(1)} = \langle \psi_{\tau n \mathbf{k}} | H_H | \psi_{\tau n \mathbf{k}} \rangle. \quad (\text{S2})$$

The Bloch state in the plane-wave basis is

$$|\psi_{\tau n \mathbf{k}}\rangle = \sum_{\mathbf{g}} u_{\tau n \mathbf{k}}^{(l)}(\mathbf{g}) |\tau, \mathbf{k} + \mathbf{g}\rangle. \quad (\text{S3})$$

Using this, we obtain

$$\Delta E_{\tau n \mathbf{k}}^{(1)} = \sum_{\mathbf{g} \neq 0} \rho_{\mathbf{g}} U_{\mathbf{g}} \sum_{\mathbf{g}'} \left[u_{\tau n \mathbf{k}}^{(l)}(\mathbf{g}') \right]^* u_{\tau n \mathbf{k}}^{(l)}(\mathbf{g}' + \mathbf{g}). \quad (\text{S4})$$

We define the form factor of the state as

$$\Lambda_{\tau n \mathbf{k}}(\mathbf{g}) = \sum_{l, \mathbf{g}'} \left[u_{\tau n \mathbf{k}}^{(l)}(\mathbf{g}') \right]^* u_{\tau n \mathbf{k}}^{(l)}(\mathbf{g}' + \mathbf{g}), \quad (\text{S5})$$

so that the energy shift becomes

$$\Delta E_{\tau n \mathbf{k}}^{(1)} = \sum_{\mathbf{g} \neq 0} \rho_{\mathbf{g}} U_{\mathbf{g}} \Lambda_{\tau n \mathbf{k}}(\mathbf{g}). \quad (\text{S6})$$

This expression provides a direct estimate of the Hartree-induced level shift in the band structure, based

on the plane-wave coefficients of the Bloch states and the density distribution.

S2. ANGLE-DEPENDENT FITTING PARAMETERS OF THE CONTINUUM MODEL

This section we provide the numerical values of the angle-dependent parameters used in the continuum model calculations presented in the main text. Table S1 lists the effective masses m_x and m_y , the intralayer moiré potential amplitudes v_{11} , v_{12} , and v_{13} together with their phases ψ_{11} , ψ_{12} , and ψ_{13} , as well as the interlayer tunneling parameters w_1 and w_2 with phases ϕ_1 and ϕ_2 . The effective masses m_x and m_y are given in units of the bare electron mass m_e , and the moiré potential amplitudes are in the unit of meV. The definitions of the intralayer moiré potential terms follow Eq. (2) of the main text, while the interlayer tunneling terms are defined in Eq. (3).

S3. HARTREE-FOCK THEORY

In this section we set up the Coulomb interaction and derive the Hartree-Fock framework used in our calculations. Our theoretical framework is based primarily on the many-body perturbation approach for moiré systems from Ref. [28]. The starting point is the band-basis Hamiltonian

$$H = H_0 + H_I, \quad (\text{S7})$$

where the non-interacting part reads

$$\mathcal{H}_0 = \sum_{s,\tau,n,\mathbf{k}} E_{\tau,n}^s(\mathbf{k}) \hat{c}_{s,\tau,n,\mathbf{k}}^\dagger \hat{c}_{s,\tau,n,\mathbf{k}}. \quad (\text{S8})$$

Here, $\hat{c}_{s,\tau,n,\mathbf{k}}^\dagger$ ($\hat{c}_{s,\tau,n,\mathbf{k}}$) creates (annihilates) an electron with momentum \mathbf{k} , spin s , valley τ , and band index n . The band dispersion is denoted by $E_{\tau,n}^s(\mathbf{k})$.

The interaction part of the Hamiltonian is given by

Stacking	θ	m_x	m_y	v_{11}	ψ_{11}	v_{12}	ψ_{12}	v_{13}	ψ_{13}	w_1	ϕ_1	w_2	ϕ_2
AA	3.89°	0.21	0.73	29.4	-22.05°	7.27	-38.24°	7.27	-38.24°	110.87	36.78°	-7.99	0°
AA	4.41°	0.21	0.73	30.29	-28.13°	5.58	-31.81°	5.58	-31.81°	108.67	37.97°	-11.06	0°
AA	5.09°	0.21	0.73	29.03	-31°	5.92	-60.45°	5.92	-60.45°	104.62	38.81°	-9.62	0°
AA	6.01°	0.21	0.73	33.28	-30.92°	4.96	-23.05°	4.96	-23.05°	101.445	39.91°	-9.61	0°
AA	7.34°	0.21	0.73	43.79	-45.36°	3.73	-8.48°	3.73	-8.48°	97.44	40.85°	-7.92	0°
AA	9.43°	0.21	0.73	56.215	-51.99°	13.29	-148.47°	13.29	-148.47°	93.43	45.13°	-10.74	0°
AB	3.89°	0.24	0.72	-20.94	0°	35.27	173.31°	35.27	-6.69°	-62.10	0°	31.80	0°
AB	4.41°	0.25	0.77	0	0°	33.90	-22.46°	33.90	157.54°	-90.78	0°	34.38	25.54°
AB	5.09°	0.25	0.69	0	0°	26.98	156.61°	26.98	-23.39°	-88.65	0°	31.43	-21.72°
AB	6.01°	0.26	0.79	0	0°	20.39	-25.72°	20.39	154.28°	-78.22	0°	27.41	20.346°
AB	7.34°	0.21	0.67	-30.92	0°	24.03	154.80°	24.03	25.20°	-79.41	0°	26.93	0°
AB	9.43°	0.21	0.71	0	0°	10.11	36.836°	11.35	135.46°	-99.12	0°	17.85	0°

TABLE S1. Angle-dependent fitting parameters of the moiré continuum model for twisted bilayer SnSe₂. The effective masses m_x , m_y are given in units of the bare electron mass m_e . The intralayer moiré potential amplitudes v_{11} , v_{12} , v_{13} and phases ψ_{11} , ψ_{12} , ψ_{13} are defined as in Eq. (2) of the main text. The interlayer tunneling parameters w_1 , w_2 and their respective phases ϕ_1 , ϕ_2 enter the tunneling term Eq. (3). These parameters are obtained by symmetry-constrained fits to DFT calculations as described in Ref. [23].

$$\mathcal{H}_1 = \frac{1}{2} \sum_{\mathbf{k}, \mathbf{k}', \mathbf{q}} \sum_{\{n_i\}} \sum_{s, s'} \sum_{\tau, \tau'} V_{\mathbf{k}, \mathbf{k}', \mathbf{q}, \{n_i\}}^{\tau \tau'} \hat{c}_{s, \tau, n_1, \mathbf{k} + \mathbf{q}}^\dagger \hat{c}_{s', \tau', n_2, \mathbf{k}' - \mathbf{q}}^\dagger \hat{c}_{s', \tau', n_3, \mathbf{k}'} \hat{c}_{s, \tau, n_4, \mathbf{k}}, \quad (\text{S9})$$

with the matrix element

$$V_{\mathbf{k}, \mathbf{k}', \mathbf{q}, \{n_i\}}^{\tau \tau'} = \sum_{\mathbf{g}} V_{\mathbf{q} + \mathbf{g}} [\Lambda_{\mathbf{k}, \mathbf{q} + \mathbf{g}}^*]_{n_4 n_1}^\tau [\Lambda_{\mathbf{k}', -\mathbf{q} - \mathbf{g}}^*]_{n_3 n_2}^{\tau'}, \quad (\text{S10})$$

where the form factor is defined as

$$[\Lambda_{\mathbf{k}, \mathbf{q} + \mathbf{g}}]_{mn}^\tau = \sum_{\mathbf{g}'} u_m^*(\mathbf{k}, \mathbf{g}'; \tau) u_n(\mathbf{k}, \mathbf{g}' + \mathbf{q} + \mathbf{g}; \tau). \quad (\text{S11})$$

In the band basis, the interaction Hamiltonian resembles the standard Coulomb interaction but with modified interaction strengths that depend on the form factors and band indices.

We then define the single-particle imaginary-time Green's function in the band basis

$$[G(\mathbf{k}, \tau)]_{\eta\eta'} = -\langle \mathcal{T}_\tau \hat{c}_{\mathbf{k}, \eta}(\tau) \hat{c}_{\mathbf{k}, \eta'}^\dagger(0) \rangle, \quad (\text{S12})$$

where $\eta = (n, s, \tau)$. Here, $\hat{c}_{\mathbf{k}, \eta}(\tau)$ and $\hat{c}_{\mathbf{k}, \eta'}^\dagger(0)$ are the annihilation and creation operators in the Heisenberg picture, \mathcal{T}_τ denotes the time-ordering operator, and $\langle \dots \rangle$ represents the thermal average over the interacting system. By performing a Fourier transform with respect to imaginary time τ , we obtain the Green's function in frequency space

$$[G(\mathbf{k}, i\omega_n)]_{\eta\eta'} = \int_0^\beta e^{i\omega_n \tau} [G(\mathbf{k}, \tau)]_{\eta\eta'} d\tau, \quad (\text{S13})$$

where $\beta = 1/(k_B T)$ is the inverse temperature, k_B is Boltzmann's constant, and $i\omega_n = (2n + 1)\pi/\beta$ are the fermionic Matsubara frequencies.

For non-interacting electrons the propagator is diagonal

$$[G_0(\mathbf{k}, i\omega_n)]_{\eta\eta'} = \frac{\delta_{\eta, \eta'}}{i\omega_n - E_{\tau, n}^s(\mathbf{k}) + \mu}, \quad (\text{S14})$$

where $E_{\tau, n}^s(\mathbf{k})$ are the eigenvalues of the single-particle Hamiltonian, and μ is the global chemical potential. The interacting Green's function, $\hat{G}(\mathbf{k}, i\omega_n)$, is determined by the Dyson equation

$$\hat{G}^{-1}(\mathbf{k}, i\omega_n) = \hat{G}_0^{-1}(\mathbf{k}, i\omega_n) - \hat{\Sigma}(\mathbf{k}, i\omega_n), \quad (\text{S15})$$

where $\hat{\Sigma}(\mathbf{k}, i\omega_n)$ represents the electron self-energy, and $\hat{G}_0(\mathbf{k}, i\omega_n)$ denotes the non-interacting Green's function. Using Feynman diagram techniques, the Hartree self-energy could be written down as

$$\hat{\Sigma}_H(\mathbf{k}, i\omega_n) = \sum_{\mathbf{g}} V_{\mathbf{g}} \hat{\Lambda}_{\mathbf{k}, \mathbf{g}}^T \frac{1}{\beta} \sum_{\mathbf{k}', m} \text{Tr} [\hat{\Lambda}_{\mathbf{k}', \mathbf{g}}^* \hat{G}(\mathbf{k}', i\omega_m)], \quad (\text{S16})$$

Similarly, for Fock self-energy

$$\hat{\Sigma}_F(\mathbf{k}, i\omega_n) = -\frac{1}{\beta} \sum_m \sum_{\mathbf{q}, \mathbf{g}} V_{\mathbf{q}+\mathbf{g}} \hat{\Lambda}_{\mathbf{k}, \mathbf{q}+\mathbf{g}}^* \times \hat{G}(\mathbf{k} + \mathbf{q}, i\omega_n - i\omega_m) \hat{\Lambda}_{\mathbf{k}, \mathbf{q}+\mathbf{g}}^T, \quad (\text{S17})$$

where we have used the relationship $\hat{\Lambda}_{\mathbf{k}+\mathbf{q}, -\mathbf{q}-\mathbf{g}} = \hat{\Lambda}_{\mathbf{k}, \mathbf{q}+\mathbf{g}}^\dagger$.

Carrying out the Matsubara summation connects the self-energy to the equal-time density matrix

$$\hat{\rho}(\mathbf{k}) = \hat{G}(\mathbf{k}, \tau = 0^-) = \frac{1}{\beta} \sum_n e^{-i\omega_n 0^+} \hat{G}(\mathbf{k}, i\omega_n). \quad (\text{S18})$$

In terms of $\hat{\rho}(\mathbf{k})$, the Hartree and Fock contributions reduce to

$$\hat{\Sigma}_H(\mathbf{k}) = \sum_{\mathbf{g}} V_{\mathbf{g}} \hat{\Lambda}_{\mathbf{k}, \mathbf{g}}^T \sum_{\mathbf{k}'} \text{Tr} \left[\hat{\Lambda}_{\mathbf{k}', \mathbf{g}}^* \hat{\rho}(\mathbf{k}') \right], \quad (\text{S19})$$

$$\hat{\Sigma}_F(\mathbf{k}) = -\sum_{\mathbf{q}, \mathbf{g}} V_{\mathbf{q}+\mathbf{g}} \hat{\Lambda}_{\mathbf{k}, \mathbf{q}+\mathbf{g}}^* \hat{\rho}(\mathbf{k} + \mathbf{q}) \hat{\Lambda}_{\mathbf{k}, \mathbf{q}+\mathbf{g}}^T, \quad (\text{S20})$$

and the total self-energy is $\hat{\Sigma}(\mathbf{k}) = \hat{\Sigma}_H(\mathbf{k}) + \hat{\Sigma}_F(\mathbf{k})$.

In practical calculations, we impose a cutoff in the band basis denoted by N . The Green's function then has dimension $(6N) \times (6N)$, accounting for spin and valley. In this study we use $N = 3$ and verify that increasing this cutoff does not qualitatively change our results.

The Hartree-Fock equations are solved iteratively: starting from a trial density matrix $\hat{\rho}_0(\mathbf{k})$, we compute $\hat{\Sigma}_H(\mathbf{k})$ and $\hat{\Sigma}_F(\mathbf{k})$, update the Green's function via Dyson's equation, and reconstruct a new $\hat{\rho}(\mathbf{k})$ until a fixed point is reached. As an initial guess, we populate the top moiré band with density matrices corresponding to different candidate phases. For the $S = 1/2$ phase, we take

$$\hat{\rho}_0(\mathbf{k}) = \begin{pmatrix} \hat{\mathbb{I}} & \hat{0} & \hat{0} \\ \hat{0} & \frac{1}{2}(\hat{\mathbb{I}} + \hat{\sigma}_z) & \hat{0} \\ \hat{0} & \hat{0} & \hat{0} \end{pmatrix}, \quad (\text{S21})$$

while for the $S = 3/2$ phase we choose

$$\hat{\rho}_0(\mathbf{k}) = \begin{pmatrix} \frac{1}{2}(\hat{\mathbb{I}} + \hat{\sigma}_z) & \hat{0} & \hat{0} \\ \hat{0} & \frac{1}{2}(\hat{\mathbb{I}} + \hat{\sigma}_z) & \hat{0} \\ \hat{0} & \hat{0} & \frac{1}{2}(\hat{\mathbb{I}} + \hat{\sigma}_z) \end{pmatrix}, \quad (\text{S22})$$

expressed in the basis $\{|\uparrow, \tau = 1, \mathbf{k}\rangle, |\downarrow, \tau = 1, \mathbf{k}\rangle, |\uparrow, \tau = 2, \mathbf{k}\rangle, |\downarrow, \tau = 2, \mathbf{k}\rangle, |\uparrow, \tau = 3, \mathbf{k}\rangle, |\downarrow, \tau = 3, \mathbf{k}\rangle\}$, where $\hat{\mathbb{I}}$ is the identity matrix.

Finally, the ground-state energy is computed using the Galitskii-Migdal expression [38],

$$E_{\text{tot}} = \frac{1}{\beta} \sum_{\mathbf{k}, n} e^{-i\omega_n 0^+} \text{Tr} \left[\left(\hat{H}_0(\mathbf{k}) + \frac{1}{2} \hat{\Sigma}(\mathbf{k}, i\omega_n) \right) \hat{G}(\mathbf{k}, i\omega_n) \right]. \quad (\text{S23})$$

When the self-energy is frequency-independent, this reduces to the simpler form

$$E_{\text{tot}} = \sum_{\mathbf{k}} \text{Tr} \left[\left(\hat{H}_0(\mathbf{k}) + \frac{1}{2} \hat{\Sigma}(\mathbf{k}) \right) \hat{\rho}(\mathbf{k}) \right]. \quad (\text{S24})$$

S4. DENSITY OF STATES FOR ADDITIONAL TWIST ANGLES

In the main text, we focused on a representative twist angle. Here we present the density of states for a range of twist angles and both stacking configurations (aligned and antialigned). The results are shown in Fig. S1 for aligned and Fig. S2 for antialigned SnSe₂.

For small twist angles $\lesssim 5^\circ$, the moiré potential strongly modifies the band structure, leading to characteristic features in the DOS such as sharp peaks associated with flat or narrow bands. The overall shapes of the DOS are qualitatively similar across different small angles, reflecting the dominance of the moiré potential over the kinetic energy scale set by the twist.

At larger twist angles, the moiré potential becomes weak compared to the kinetic energy. In this regime, the difference between aligned and antialigned stacking is greatly reduced, and the DOS gradually approaches that of an anisotropic two-dimensional electron gas. This crossover is consistent with the Lifshitz transition discussed in the main text, where the Fermi surface evolves between layer-polarized and layer-hybridized states as a function of V_z .

Thus, the angle dependence of the DOS confirms that strong moiré features appear only at relatively small twist angles, while at larger angles the low-energy properties are essentially determined by the parent band anisotropy with only weak stacking dependence.

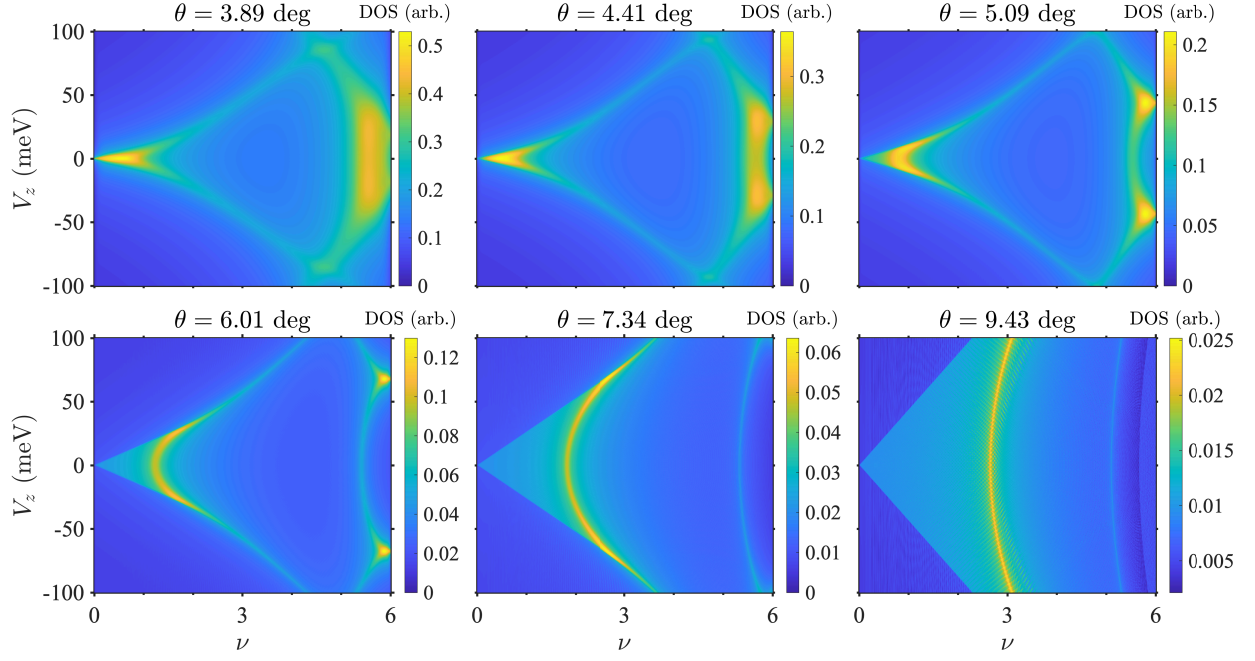


FIG. S1. Density of states of the non-interacting model for aligned SnSe₂ at different twist angles. For twist angles $\theta \lesssim 5^\circ$, where the moiré effect is strong, the density of states shows qualitatively similar features. At larger twist angles, the difference between aligned and antialigned stacking is reduced, since the moiré potential becomes weak compared to the kinetic energy scale set by the twist. This behavior is consistent with the Lifshitz transition $\nu \propto |V_z|$ between layer-polarized and layer-hybridized regimes.

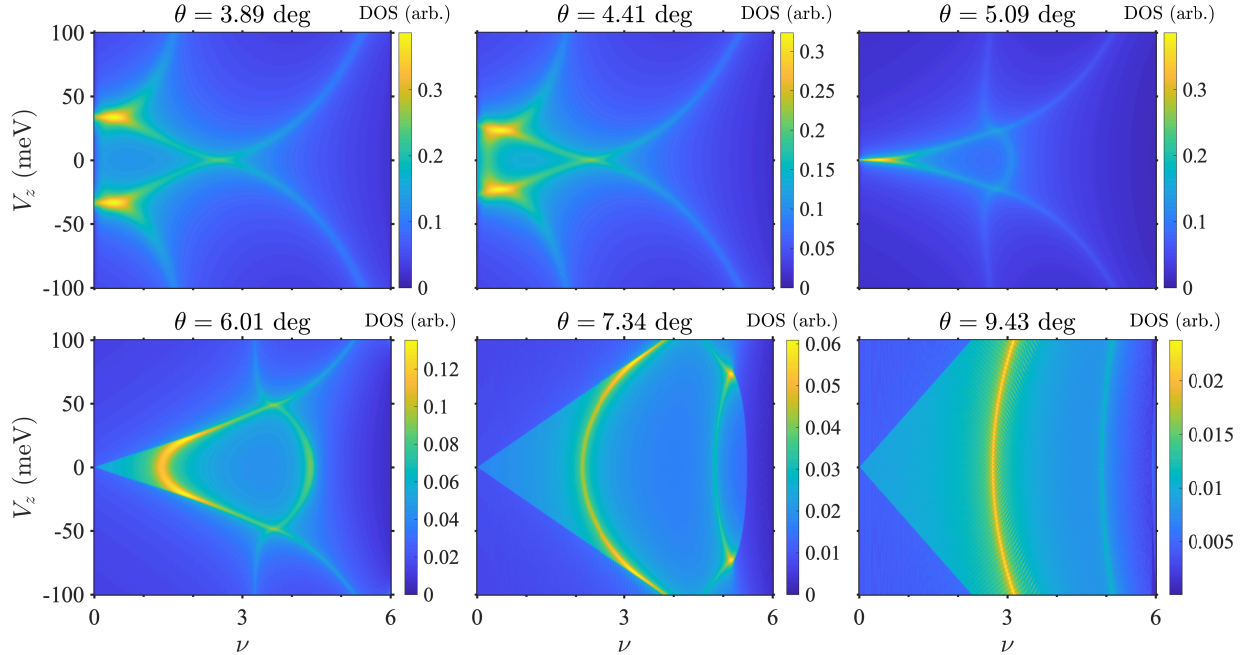


FIG. S2. Density of states of the non-interacting model for antialigned SnSe₂ at different twist angles. For twist angles $\theta \lesssim 5^\circ$, where the moiré effect is strong, the density of states shows qualitatively similar features. At larger twist angles, the difference between aligned and antialigned stacking is reduced, since the moiré potential becomes weak compared to the kinetic energy scale set by the twist. This behavior is consistent with the Lifshitz transition $\nu \propto |V_z|$ between layer-polarized and layer-hybridized regimes.